Computer-aided diagnostic detection system of venous beading in retinal images

Ching-Wen Yang
Taichung Veterans General Hospital
Taichung, Taiwan

Dye-Jyun Ma
Shuenn-Ching Chao
National Chung-Hsing University
Taichung, Taiwan

Chuin-Mu Wang
National Cheng-Kung University
Department of Electrical Engineering
Tainan, Taiwan

Chia-Hsin Wen
Taichung Veterans General Hospital
Taichung, Taiwan

Chien-Shun Lo
Pau-Choo Chung
National Cheng-Kung University
Department of Electrical Engineering
Tainan, Taiwan

Chein-I Chang, MEMBER SPIE
University of Maryland—Baltimore County
Department of Computer Science
and Electrical Engineering
Baltimore, Maryland 21250
E-mail: cchang@umbc.edu

Abstract. The detection of venous beading in retinal images provides an early sign of diabetic retinopathy and plays an important role as a preprocessing step in diagnosing ocular diseases. We present a computer-aided diagnostic system to automatically detect venous beading of blood vessels. It comprises of two modules, referred to as the blood vessel extraction module (BVEM) and the venus beading detection module (VBDM). The former uses a bell-shaped Gaussian kernel with 12 azimuths to extract blood vessels while the latter applies a neural network-based shape cognitron to detect venous beading among the extracted blood vessels for diagnosis. Both modules are fully computer-automated. To evaluate the proposed system, 61 retinal images (32 beaded and 29 normal images) are used for performance evaluation.
 [S0091-3286(00)01305-2]

Subject terms: bell-shaped Gaussian matched filter; blood vessel extraction module; detection; extraction; neural network; retinal images; shape cognitron; venus beading detection module.

Paper ATR-014 received Sep. 3, 1999; revised manuscript received Nov. 23, 1999; accepted for publication Dec. 9, 1999.

1 Introduction

Retinal (or fundus) images provide information about the blood supply system of the retina. The information about blood vessels (veins) can be used to assess the severity of retinal diseases such as diabetic retinopathy, hypertension, and various vascular disorders. In addition, blood vessels are also used as landmarks for localizing the optic nerve, the fovea, and lesions or as a measure for abnormalities in diameter, color, and tortuosity. For example, the diameter of a vein with beading and the diameter of a normal vein are different. Thus, a reliable assessment of variations in vessel diameters can be used as a guideline of the degree of venous beading for an early stage treatment.[1] A beaded vein exhibits periodic changes in diameter along its length and shape that look like a string of sausages.[2,3] The beads have diameters that do not decrease monotonically with the distance from macula. Fig. 1 shows a typical shape of a normal vein and a sausage-shaped beaded vein. Compared to other types of retinal abnormalities, venous beading is an effective indicator of diabetic retinopathy.[4]

Previous works on the analysis of retinal images have been primarily focused on extraction of blood vessels and microaneurysms, where the retinal images are acquired digitally or digitized by scanning slice films into digital forms. Techniques include thresholding and morphological edge detectors.[5–7] The idea of using thresholding is based on the fact that the intensities of the veins and the background are different so that veins can be extracted from the background by thresholding. Morphological edge detectors were proposed to find edges between the background and veins to contour the blood vessels. Unfortunately, both approaches may suffer from drawbacks such as illumination problems in retinal images and poor local contrast of blood vessels.

Tanaka and Tanaka suggested an adaptive thresholding method followed by binary thinning to detect vessels.[8] Recently, Chaudhuri et al. made use of a set of convolution masks to extract blood vessels in retinal images by rotating a linear feature detector of a Gaussian cross section.[9] Lay and Badouin applied a morphological transformation of an image to extract microaneurysms so that the number of microaneurysms can be used as a measure for grading the severity of diabetic retinopathy.[10] In addition, other techniques were also developed for different purposes. For instance, automatic registration of retinal images enables us to accurately compare images taken at different times and further gives us an ability to calculate changes in both le-

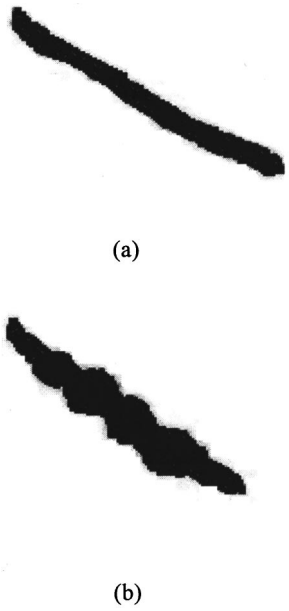

Fig. 1 (a) Normal vein and (b) beaded vein.

sions and normal anatomic structure.[11] Fluorescein angiography is a well-known clinical technique that has been used to differentiate retinal diseases and determine if a laser treatment of retina is necessary.[12] Detection of nonperfused zones in a retinal image is also useful for detecting and monitoring diabetic retinopathy in an early stage.[13]

Diabetic retinopathy has shown a great influence on adults in developing countries. One of most serious damages to retina is blindness. Thus, detection and prevention of diabetic retinopathy are extremely important. A specific pathology called venous beading is known as a good indicator of the degree of diabetic retinopathy.[4] We present a computer-automated diagnostic system that can be used to detect venous beading in retinal images. The proposed system is made up of two diagnostic system modules, referred to as the blood vessel extraction module (BVEM) and the venus beading detection module (VBDM).

The BVEM first uses a bell-shaped Gaussian matched filter (BSGMF), then a joint relative entropy (JRE) thresholding method[14,15] to extract blood vessels as an initial step for venous beading detection. The BSGMF improves Chaudhuri et al.'s[9] Gaussian matched filter. Since the extracted blood vessels generally may be noisy and have rough edges, two morphological operators, dilation and erosion, are also included to smooth the detected edges as well as to suppress noise. The resulting blood vessels are then further processed by a thinning method[16] to find and locate their branching points that must be removed prior to the VBDM. These branching points generally provide no value in venous beading detection but create a difficulty for the shape cognitron implemented in the VBDM. Nevertheless, note that in some case these branching points can be useful, such as in the algorithm developed in Ref. 17.

The objective of the VBDM is to make a diagnosis based on blood vessels extracted by the BVEM. It includes a neural network-based shape cognitron.[18] The shape cognitron was originated from a tricognitron[19,20] and was particularly developed for shape analysis. It has found application in classification of clustered microcalcifications.[21] It converts a two-dimensional (2-D) pattern to a three-dimensional (3-D) figure pattern from which its shape curvatures can be extracted to generate a set of shape features for classification. These features can be used to classify extracted blood vessels into different degrees of venous beading. To see the performance of the proposed computer aided venous detection system, 61 retinal images including 32 with venous beads and 29 normal cases are used for evaluation. The experiments demonstrate the potential usefulness of the system in the detection of venous beading.

This paper is organized as follows. Section 2 describes the BVEM which implements a sequence of processes including bell-shaped Gaussian matched filtering, joint relative entropy thresholding, morphological operations, and thinning. Section 3 presents the VBDM, where the shape cognitron is developed to discriminate venous beaded veins from normal vessels. Section 4 reports experiments conducted to evaluate the entire diagnostic system for potential utility in clinical applications. Finally, Sec. 5 presents brief concluding remarks.

2 BVEM

Extracting blood vessels is a crucial step for diagnosis of venous beading detection. This section presents the first system module of an automatic diagnostic detection of venous beading, the BVEM. The BVEM can be implemented in four sequential stages: extraction of blood vessels, segmentation of the extracted blood vessels, edge smoothing of extracted blood vessels and noise suppression, and detection and elimination of branching points. Throughout this paper, the terms vessel and vein are used interchangeably.

2.1 *Extraction of Blood Vessels by BSGMF*

Blood vessels generally do not have ideal step edges and the intensity profile in every vessel varies. Nevertheless, gray-level values of a blood vessel can be approximated by a Gaussian curve[9]:

$$f(x,y)=A\left[1\pm K\exp\left(-\frac{d^2}{2\sigma^2}\right)\right], \tag{1}$$

where d is the perpendicular distance between the pixel at (x,y) and the centerline of the blood vessel, σ defines the spread of the intensity profile, A is the gray-level intensity of the local background, and K is a constant used to account for the reflectance of the blood vessel relative to its neighborhood. Note that the notation $\pm$ in Eq. (1) represents two categories of retinal images to be considered. The plus indicates fluorescence angiography, where patients are injected by fluorescence, as opposed to the minus, which corresponds to no fluorescence injected into patients. Based on Eq. (1), Chaudhuri et al. derived a 2-D Gaussian θ angle-matched filter kernel given by

$$K_\theta(x,y)=\pm\exp\left(-\frac{u^2}{2\sigma^2}\right), \tag{2}$$

0	0	0	0	0	0	0	0	0	0	0	0	0	0	0
0	0	0	0	0	0	0	2	0	0	0	0	0	0	0
0	0	0	0	2	2	2	2	2	2	2	0	0	0	0
0	0	0	2	2	1	1	1	1	1	2	2	0	0	0
0	0	2	2	1	0	-1	-1	-1	0	1	2	2	0	0
0	0	2	1	0	-1	-3	-4	-3	-1	0	1	2	0	0
0	0	2	1	-1	-3	-6	-7	-6	-3	-1	1	2	0	0
0	2	2	1	-1	-4	-7	-8	-7	-4	-1	1	2	2	0
0	0	2	1	-1	-3	-6	-7	-6	-3	-1	1	2	0	0
0	0	2	1	0	-1	-3	-4	-3	-1	0	1	2	0	0
0	0	2	2	1	0	-1	-1	-1	0	1	2	2	0	0
0	0	0	2	2	1	1	1	1	1	2	2	0	0	0
0	0	0	0	2	2	2	2	2	2	2	0	0	0	0
0	0	0	0	0	0	0	2	0	0	0	0	0	0	0
0	0	0	0	0	0	0	0	0	0	0	0	0	0	0

Fig. 2 Typical mask used to implement BSGMF with $\sigma=2$.

where $(u,v)^T$ is a new coordinate of $(x,y)^T$ after $(x,y)^T$ is rotated by θ angle. In other words, if we let $\mathbf{R}(\theta)$ be the rotation matrix specified by θ, then

$$\mathbf{R}(\theta)=\begin{bmatrix}\cos\theta & -\sin\theta\\ \sin\theta & \cos\theta\end{bmatrix}, \tag{3}$$

and $(u,v)^T=(x,y)^T\mathbf{R}(\theta)$. Chaudhuri et al. used Eq. (2) to design 12 2-D Gaussian θ angle-matched filter kernels $\{K_{\theta_i}(x,y)\}_{i=0}^{11}$ to cover 12 orientations of a blood vessel from angles $\theta_0=0$ deg, $\theta_2=15$ deg,…, to $\theta_{11}=165$ deg, where the difference between two consecutive angles is 15 deg, i.e., $\theta_{i+1}-\theta_i=15$ deg.

One drawback of Chaudhuri et al.'s approach is high computational complexity. It requires separate implementations of 12 kernels $\{K_{\theta_i}(x,y)\}_{i=0}^{11}$. To mitigate this problem, a BSGMF was developed to cover all 12 orientations,[22] where the designed kernel was given by

$$K(x,y)=\pm\exp\left(-\frac{x^2+y^2}{2\sigma^2}\right), \tag{4}$$

with the tail truncated at $x^2+y^2=3\sigma^2$. Equation (4) is not a low-pass filter, but rather a bell-shape Gaussian filter. As noted in Ref. 9, it was an effective filter to detect bell-shaped objects. Since the new kernel has a Gaussian shape along every direction that makes it look like a bell, it is named the BSGMF. To implement the BSGMF, its coefficients are each multiplied by a scale factor of 10 and rounded off to their nearest integer. A typical bell-shaped kernel with $\sigma=2$ is shown in Fig. 2 and the result is shown in Figs. 3(a) and 3(b) where Fig. 3(a) is the original image and Fig. 3(b) is the resulting BSGMF-processed image. As we can see, the blood vessels have been extracted.

2.2 *Segmentation of Extracted Blood Vessels by JRE Thresholding*

This section proposes a relative entropy-based thresholding method to segment the blood vessels extracted by BSGMF from the background. It is based on the concept of the gray-level co-occurrence matrix defined next.

2.2.1 *Gray-level co-occurrence matrix*

Given a digital image of size $M\times N$ with L gray levels denoted by $G=\{0,1,...,L-1\}$, let $f(x,y)$ be the gray level of the pixel at the spatial location (x,y). Then the image can be represented by a matrix $\mathbf{F}=[f(x,y)]_{M\times N}$. A co-occurrence matrix of an image is an $L\times L$ square matrix, denoted by $\mathbf{W}=[t_{ij}]_{L\times L}$, where t_{ij} is the number of transitions from gray level value i to gray level value j defined as follows[14]:

$$t_{ij}=\sum_{m=1}^{M}\sum_{n=1}^{N}\delta_{mn}, \tag{5}$$

with

$$\delta_{mn}=1 \quad \text{if} \begin{bmatrix} f(m,n)=i \ \text{ and } \ f(m+n+1)=j \\ \text{and/or} \\ f(m,n)=i \ \text{ and } \ f(m+n+1)=j \end{bmatrix}$$
$$=0 \quad \text{otherwise.} \tag{6}$$

Note that the co-occurrence matrix just defined considers only the pixel on the right transition as well as the pixel below transition since it has been found that including the pixels on the left of and above the transition does not provide significant information and improvement.

Normalizing the total number of transitions in the co-occurrence matrix, a desired transition probability from gray level i to j is obtained by

$$p_{ij}=\frac{t_{ij}}{\sum_{k=0}^{L-1}\sum_{l=0}^{L-1}t_{kl}}. \tag{7}$$

Assuming that t is a value used to threshold an image, t partitions the co-occurrence matrix defined by Eq. (5) into four quadrants, A, B, C, and D, as shown in Fig. 4. These four quadrants can be further grouped into two classes. If we assume that pixels with gray levels above the threshold are assigned to the foreground (objects), and those with gray levels equal to or below the threshold are assigned to the background, quadrants A and C correspond to local transitions within background (B), denoted by BB and foreground (F), denoted by FF, respectively, as shown in Fig. 4. Similarly, quadrants B and D represent transitions across boundaries between background and foreground, thus, they can be denoted by BF and FB, respectively. Thus, if we let $G_0=\{0,...,t\}$ and $G_1=\{t+1,...,L-1\}$, the four quadrants A(BB), B(BF), D(FB), and C(FF) are determined by the gray-level ranges $G_0\times G_0$, $G_0\times G_1$, $G_1\times G_0$, and $G_1\times G_1$, respectively. Then the probabilities associated with each quadrant can be obtained by

$$P_A^t=\sum_{i=0}^{t}\sum_{j=0}^{t}p_{ij}, \quad P_B^t=\sum_{i=0}^{t}\sum_{j=t+1}^{L-1}p_{ij},$$
$$P_C^t=\sum_{i=t+1}^{L-1}\sum_{j=0}^{t}p_{ij}, \quad P_D^t=\sum_{i=t+1}^{L-1}\sum_{j=t+1}^{L-1}p_{ij}. \tag{8}$$

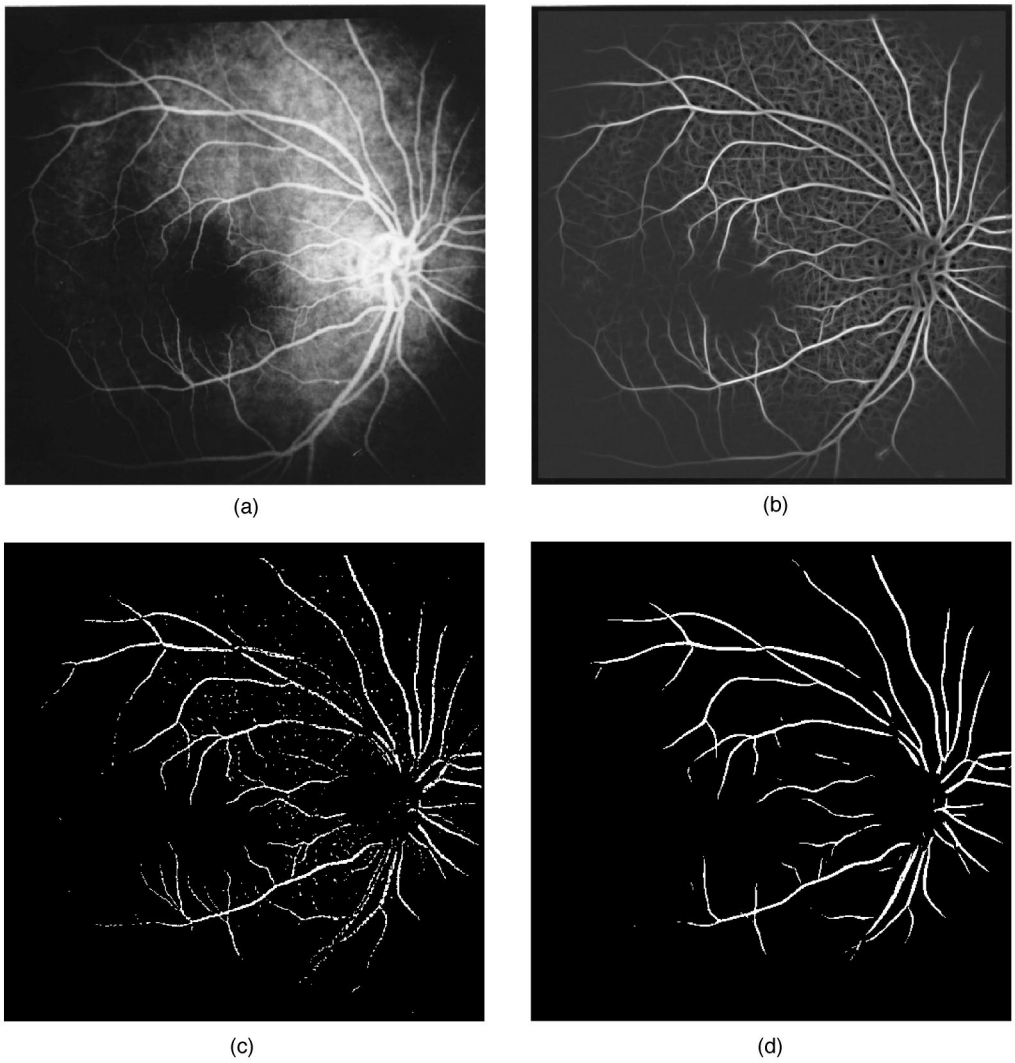

Fig. 3 (a) Original image, (b) BSGMF-processed image of Fig. 3(a), (c) JRE-thresholded image of Fig. 3(b), and (d) noise-suppressed image of Fig. 3(c).

The probabilities in each quadrant can be further obtained by so-called ''cell probabilities'':

$$p^t_{ij|A}=\frac{p_{ij}}{P^t_A}, \quad p^t_{ij|B}=\frac{p_{ij}}{P^t_B}, \quad p^t_{ij|C}=\frac{p_{ij}}{P^t_C}, \quad p^t_{ij|D}=\frac{p_{ij}}{P^t_D}, \qquad (9)$$

which are probabilities conditioning on specific quadrants.

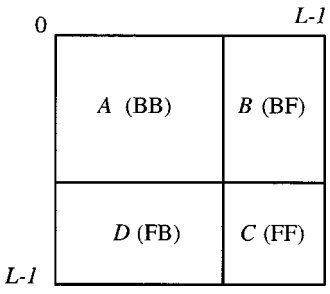

Fig. 4 Four quadrants of a co-occurrence matrix W.

2.2.2 *JRE thresholding*

Relative entropy has been used to measure the information distance between two sources. The smaller the relative entropy, the more closer the two sources in terms of their probability distributions. Let two sources with L symbols be described by probability distributions $\mathbf{p}=(p_1,\ldots,p_L)$ and $\mathbf{h}=(h_1,\ldots,h_L)$, respectively. The relative entropy between $\mathbf{p}$ and $\mathbf{h}$ (or the entropy of $\mathbf{h}$ relative to $\mathbf{p}$) denoted by $J(\mathbf{p};\mathbf{h})$ is defined by

$$J(\mathbf{p};\mathbf{h})=\sum_{j=0}^{L-1} p_j \log\frac{p_j}{h_j}. \qquad (10)$$

The definition given by Eq. (10) was first introduced by Kullback[23] as an information distance measure between two probability distributions. Therefore, it is known as Kullback-Leiber's information discriminant measure, cross entropy, and directed divergence. As the definition implies, the smaller the relative entropy, the less the discrepancy between $\mathbf{p}$ and $\mathbf{h}$, thus, the better the match between $\mathbf{p}$ and

h. Note that the relative entropy is not symmetric. In this paper, the original image is always designated as the nominal image **p** and the thresholded image is the one (i.e., **h**) that tries to match it.

The definition in Eq. (10) is based on the image gray-level histogram and does not exploit the spatial dependency of the pixel values in the image. This leads to an idea of using co-occurrence matrix to extend their first-order relative entropy specified by Eq. (10) to a second-order JRE. In doing so, we assume that t is the selected threshold. By assigning 1 to all gray levels in $G_1=\{t+1,...,L-1\}$ and 0 to all gray levels in $G_0=\{0,...,t\}$, we obtain a binary image and its associated co-occurrence matrix $[h_{ij}^t]$ with h_{ij}^t for each quadrant given by

$$h_{ij|A}^t=q_A^t=\frac{P_A^t}{(t+1)(t+1)} \quad \text{for} \quad i,j\in G_0, \tag{11}$$

$$h_{ij|B}^t=q_B^t=\frac{P_B^t}{(t+1)(L-t-1)} \quad \text{for} \quad i\in G_0 \quad \text{and} \quad j\in G_1, \tag{12}$$

$$h_{ij|C}^t=q_C^t=\frac{P_C^t}{(L-t-1)(L-t-1)} \quad \text{for} \quad i\in G_1 \quad \text{and} \quad j\in G_1, \tag{13}$$

$$h_{ij|D}^t=q_D^t=\frac{P_D^t}{(L-t-1)(L+1)} \quad \text{for} \quad i\in G_1 \quad \text{and} \quad j\in G_0, \tag{14}$$

where the gray levels in G_0 and G_1 are treated equally likely in probability and P_A^t, P_B^t, P_C^t, and P_D^t are defined by Eq. (8). Despite that the thresholded binary image has only gray level values 0 (background) and 1 (foreground), note that the subscript of h_{ij}^t, ij corresponds to the same ij, the subscript of p_{ij}. For each selected t, $h_{ij|A}^t$, $h_{ij|B}^t$, $h_{ij|C}^t$, and $h_{ij|D}^t$ are constants in each individual quadrant and depend only on the quadrants to which they belong. Therefore, they can be denoted by q_A^t, q_B^t, q_C^t, and q_D^t, respectively. Using Eqs. (7) and (11) to (14), Eq. (10) can be simplified as

$$\begin{aligned} J(\{p_{ij}\};\{h_{ij}^t\}) &= \sum_{i=0}^{L-1}\sum_{j=0}^{L-1} p_{ij}\log\frac{p_{ij}}{h_{ij}^t} \\ &= -H(\{p_{ij}\})-\sum_{i,j} p_{ij}\log h_{ij}^t, \end{aligned} \tag{15}$$

where $H(\{p_{ij}\})$ is the entropy of $\{p_{ij}\}_{i=0,j=0}^{L-1,L-1}$ defined by $H(\{p_{ij}\})=-\Sigma_{i=0}^{L-1}\Sigma_{j=0}^{L-1}p_{ij}\log p_{ij}$ and independent of t. Thus, minimizing the relative entropy of Eq. (15) is equivalent to minimizing the second term of Eq. (15), which can be further reduced to maximizing:

$$P_A^t\log q_A^t+P_B^t\log q_B^t+P_C^t\log q_C^t+P_D^t\log q_D^t. \tag{16}$$

This implies that in order to obtain a desirable threshold to segment the foreground from the background, we only have to maximize Eq. (16) over t. As mentioned previously, however, quadrants B and D describe the activities of transitions between background and foreground. Therefore, maximizing only

$$P_B^t\log q_B^t+P_D^t\log q_D^t, \tag{17}$$

rather than Eq. (16), was shown to be more effective in edge detection.[15] This results in JRE thresholding method, which finds a threshold t_{JRE} such that it satisfies

$$t_{\mathrm{JRE}}=\arg[\min_{t\in G} H_{\mathrm{JRE}}(t)], \tag{18}$$

where $H_{\mathrm{JRE}}(t)$ is defined as $H_{\mathrm{JRE}}(t)\equiv-(P_B^t\log q_B^t+P_D^t\log q_D^t)$ via Eq. (17). Note that $H_{\mathrm{JRE}}(t)$ is taken over all pixels with gray levels falling in BF and FB. Figure 3(c) shows the result of applying JRE to the BSGMF-processed image in Fig. 3(b); the extracted blood vessels have been enhanced and segmented from the background.

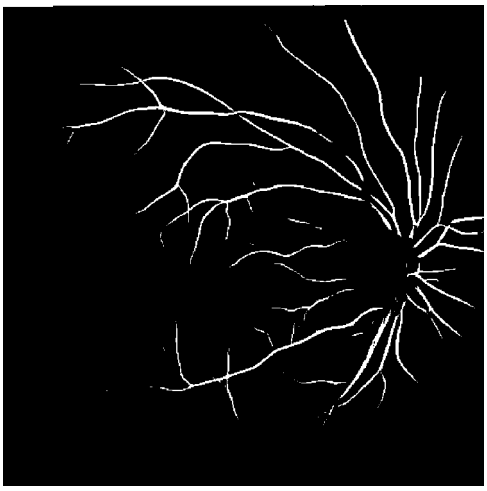

Fig. 5 Results of Fig. 3(a) using Chaudhuri et al.'s Gaussian matched filter.

2.3 *Edge Smoothing and Noise Suppression*

Since the BSGMF uses only one bell-shaped Gaussian kernel to match all possible orientations of blood vessels, the extracted blood vessels may have more rougher edges than those obtained by Chaudhuri et al.'s 12 2-D Gaussian θ angle-matched filter kernels $\{K_{\theta_i}(x,y)\}_{i=0}^{11}$. This is demonstrated by a comparison of the images between Fig. 3(c) and Fig. 5, where the image in Fig. 5 was generated by Chaudhuri et al.'s method. However, this shortcoming can be remedied by morphological dilation and erosion.

As shown in Fig. 3(c), there are many small white spots resulting from the BSGMF. These could be noise or microaneurysms and should be removed. Morphological opening can be used for this purpose. It consists of a dilation followed by an erosion. Both operations are performed with the same structuring element, as shown in Fig. 6. The size and shape of an appropriate structuring element are generally determined by the resolution of an image of in-

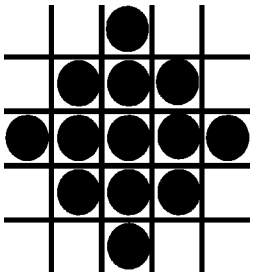

Fig. 6 Structuring element.

terest. Figure 3(d) results from a morphological opening applied to the image in Fig. 3(c) with the structuring element given by Fig. 6. As shown in Fig. 3(d), all noiselike white dots and some small vessels were removed. It is worth noting that small vessels could be also extracted by appropriately adjusting the variance used in BSGMF. Since venous beading usually occurs at larger blood vessels, removal of small vessels does not cause any misdiagnosis.

2.4 *Finding Elimination of Branching Points*

Because of nonuniform blood flow pressure the shapes of veins near branches are generally not regular. This phenomenon is not caused by diabetic retinopathy, but could be mistakenly viewed as venous beads. One way to resolve this problem is vein skeletonization by thinning. This can be accomplished by a thinning algorithm proposed in Ref. 16. It uses a 3×3 window centered at the pixel of interest, denoted by C. Then its eight neighboring pixels in the window can be defined in accordance with its compass directions, E (east), S (south), W (west), N (north), SE (southeast), SW (southwest), NE (northeast), and NW (northwest). We further define vX to be the logical function of the pixel X, which takes only two values, true and false, and eX to be the logical function of the pixel X, which takes the value true only if C is on the edge of a vein. Furthermore, a pixel is defined to be an edge pixel if it has two to six neighbors. The thinning criterion is to remove C if the pixel C is on a vein edge. More specifically, C will be removed if the following statement is false

$$vC\cdot[\neg(eC)+(eE\cdot vN\cdot vS)+(eS\cdot vW\cdot vE)+(eE\cdot eSE\cdot eS)], \tag{19}$$

where ''¬,'' ''·,'' and ''+'' denote logical NEG, AND, and OR, respectively. In some cases, midline elements may show staircases resulting from the thinning algorithm. For instance, Fig. 7(a) shows an example of a staircase on the right, which is supposed to be midline elements on the left. Thus, a final cleanup processing may be necessary, as proposed in Ref. 16.

As mentioned previously, the purpose of thinning is to find branching points so that the caused bifurcations can be eliminated prior to venous beading detection. After thinning, a point with three or more neighboring points is considered to be a branching point. These branching points can be identified as ''fork'' points, i.e., Y-shaped points in the skeleton image produced by the preceding thinning process. An example of two types of such fork points is provided in Fig. 7(b). As soon as a branching point is identified, we place a square window mask with the center at the branching point and eliminate all vascular pixels in the square including the branching point. How many neighboring points must be eliminated depends on the size of extracted blood vessels. In our experiments a 9×9 square window mask was used. Figures 8(a) and 8(b) illustrate these operations. Figure 8(b) shows an image after being thinned with the fork points eliminated.

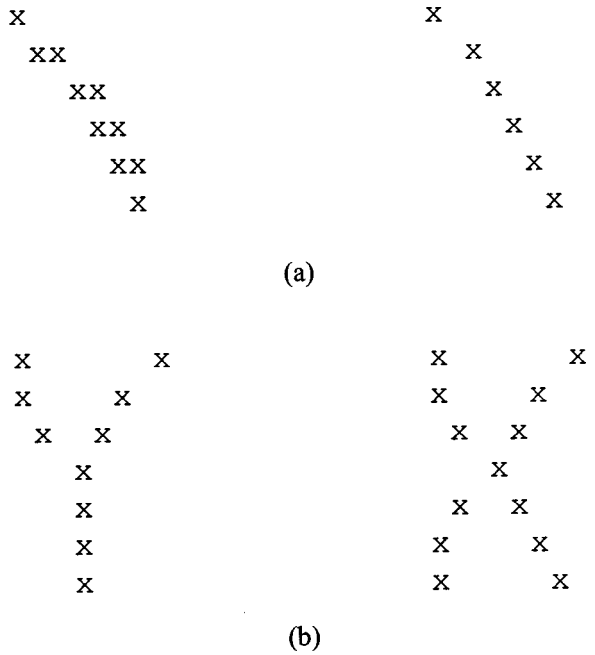

Fig. 7 (a) Example of how midline elements may show a staircase and (b) example of two types of fork points.

3 VBDM

The BVEM only produces an image showing blood vessels with all bifurcations removed. It does not provide any means to detect venous beads; hence, this section develops a VBDM. The major component of the VBDM is the shape cognitron (SC), which was originally devised to recognize shape patterns of microcalcifications in mammograms.

3.1 *SC*

The SC is derived from the tricognitron[19,20] and Fukushima and Wake's necognitron.[24] It was particularly designed to classify clustered microcalcifications into malignant and benign, using a set of shape features it generates. It is known that malignant clustered microcalcifications generally have irregular shapes as opposed to round-shaped or egg-shaped benign clustered microcalcifications. SC captures the shape curvatures of clustered microcalcifications and provides a crucial indication of malignancy.[21] Since this mammographic characteristic is also similar to that of venous beading, the SC is modified for this purpose. Using a set of orientation patterns as templates, the SC is able to generate a hexadecimal number for each pixel that represents a shape curvature at this pixel, as shown in Table 1. Due to the fact that venous beading generally has an irregular shape, these shape curvature representations provide

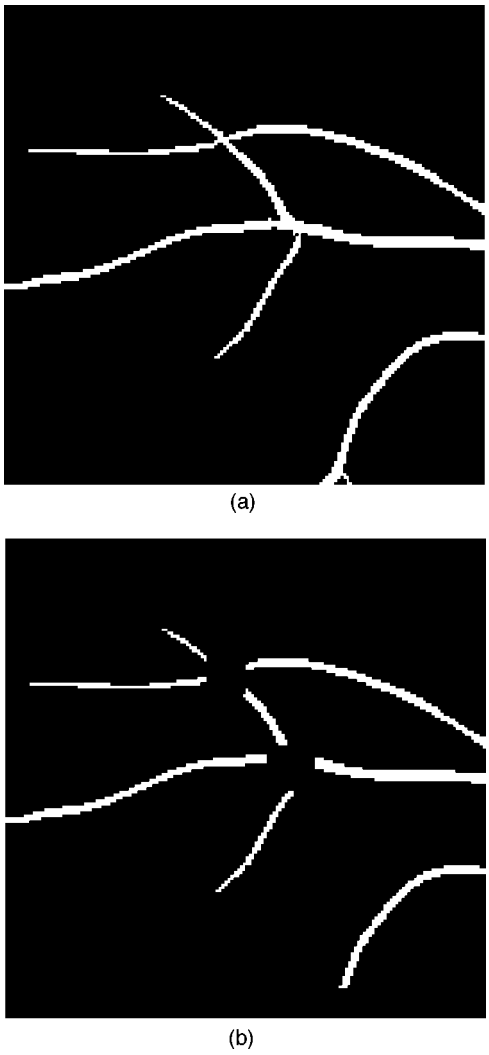

Fig. 8 (a) Original vascular pattern with two branching points and (b) two branching points are removed from (a).

very useful information to differentiate a venous beaded vein from a normal vein. From this shape curvature information, a set of shape features can be generated, as shown in Table 2, and used as training data for the subsequent neural network-based classifier for diagnosis.

The SC is a neural network-like system (as shown in Fig. 9) and consists of two modules, each of which has two layers, called the simple layer and the complex layer. Between these two modules is a layer called the 3-D figure layer. The first module is similar to that used in the neocognitron.[24] It uses eight shape spatial patterns that can be represented by 3×3 masks, each of which specifies an orientation using a particular spatial patterns. Figure 10 shows eight different geometric patterns corresponding to various orientations, 22.5 deg (i.e., <45 deg) and 45, 90, 135, 180, 225, 270, and 360 deg. The objective of the first module is to capture these geometric shape orientations of an input pattern into numeric values, which will be used to represent eight specific orientation spatial patterns. To do so, it implements a two-layer operation, a simple layer denoted by S_1 and a complex layer denoted by C_1. Layer S_1 contains 20 cell planes of size 20×20, resulting from three series of weighting window masking processes operating on the input pattern. Layer C_1 contains eight cell planes of size 20×20 obtained by merging 20 cell planes in layer S_1. They are results of different weight assignments generated by the window masking processing in layer S_1 and the merging procedure in layer C_1. The layer following the first module is the 3-D figure layer, which is a feature extraction-display layer that extracts and stores the information of the shape orientations of an input pattern in the third dimension. It displays the input pattern as a 3-D figure using these numeric representations as elevation of the pattern to show orientations in the third dimension. The second module can be viewed as a joint feature selection and classification system that is made up of a feature selection layer S_2, which generates a desired set of shape features from the 3-D figure layer, and a classification layer C_2, which employs a backpropagation neural network (BNN) as a classifier with the shape features produced by layer S_2 as inputs. The second simple-complex layer (S_2,C_2) is a shape feature selection-classification unit where layer S_2 is the feature selection layer and the layer C_2 is the classification layer. The task of layer S_2 is to integrate and select shape orientations obtained from the 3-D figure layer, and generate a desired set of shape features based on certain classification criteria. Layer C_2 employs a neural network as a classifier to produce final classification results. The objective of introducing the 3-D figure layer between the (S_1,C_1) unit and (S_2,C_2) unit originates from the tricognitron. It is a 3-D figure layer thus has only one $20\times20\times20$ cell cube. It displays a 2-D 20×20 input pattern as a 3-D $20\times20\times20$ figure, where the numeric value assigned to each pixel in the input pattern represents the shape orientation of that pixel. This numeral is generated by the weights produced by the first unit and can be viewed as the elevation of the pixel when the pattern is displayed as a 3-D figure. The details of each layer are described as follows.

Table 1 Shape curvature generated by the SC.

Shape Curvature (deg)	Number
<45	2
45	3
90	4
135	5
180	6, 7
225	8, 9
270	*a*, *b*
360	*c*

3.1.1 *Input layer U_0 of SC*

The input layer denoted by U_0 receives a 2-D pattern specified by a 20×20 cell plane with an example shown in Fig. 11 for illustration.

Table 2 A set of features and their corresponding descriptions.

Feature Number	Feature Name	Description
1	Vein number	The number of the vascular branches
2	Total perimeter	Sum(2, 3, 4, 5, 7, 9)
3	Total length	The total length of all vascular branches
4	Irregularity degree	$\frac{\text{sum(2,3,4)}}{\text{total perimeter}}$
5	Radian degree	$\frac{\text{sum(4,5,9)}}{\text{total perimeter}}$
6	Smooth degree I	$\frac{\text{sum(7)}}{\text{total perimeter}}$
7	Smooth degree II	$\frac{\text{sum(7 with two or more neighbors=7)}}{\text{total perimeter}}$
8	Average irregularity degree	$\frac{\text{sum(2,3,4)}}{\text{vein numbers}}$
9	Average radian degree	$\frac{\text{sum(4,5,9)}}{\text{vein numbers}}$
10	Average smooth degree I	$\frac{\text{sum(7)}}{\text{vein numbers}}$
11	Average smooth degree II	$\frac{\text{sum(7 with two or more neighbors=7)}}{\text{vein numbers}}$
12	Ratio *b* without neighbor 7	$\frac{\text{sum(}b\text{ without neighbors=7)}}{\text{sum(}b\text{)}}$
13	Ratio of *b* and the perimeter	$\frac{\text{sum(}b\text{ without neighbors=7)}}{\text{total perimeter}}$

3.1.2 *First module* (S_1, C_1) *of the SC: a combined simple* S_1 *layer and complex* C_1 *layer*

Basically, the first module is a combined simple-complex layer (S_1, C_1). It is a shape-orientation conversion unit that converts the shape orientation information from the input pattern to a numeric representation for each pixel and passes it on to the 3-D figure layer, which is a shape-orientation extraction-display layer. Layer S_1 contains 20 20×20 cell planes, responding to the input pattern. It makes use of 20 masking window patterns (shown in Fig.

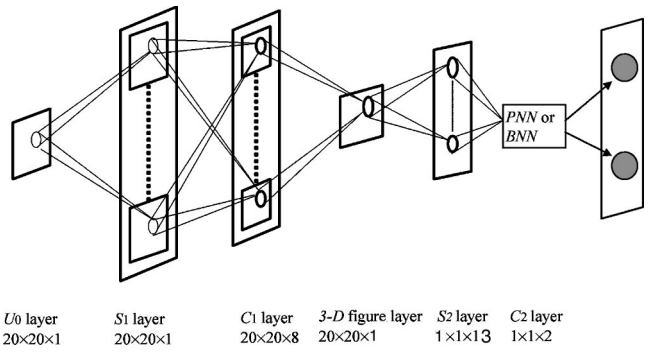

Fig. 9 Structure of the SC.

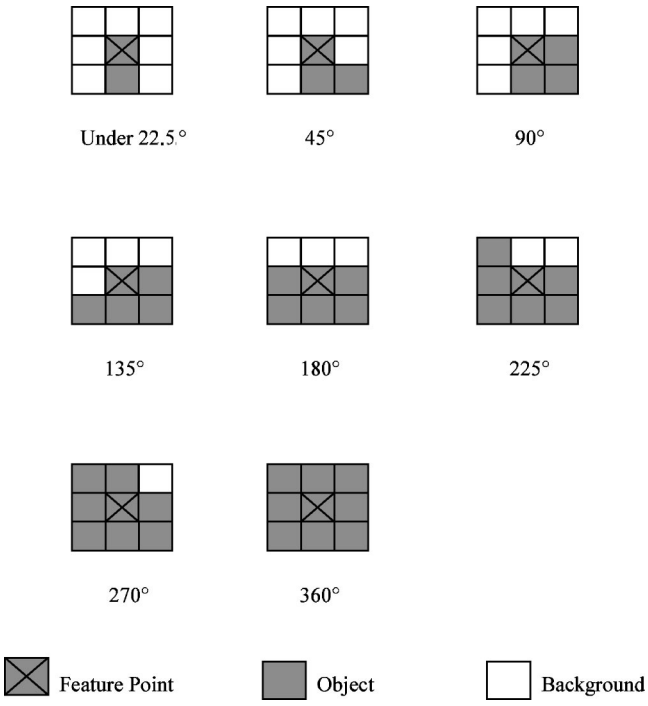

Fig. 10 Using 3×3 masks to represent various degrees of shape curvatures.

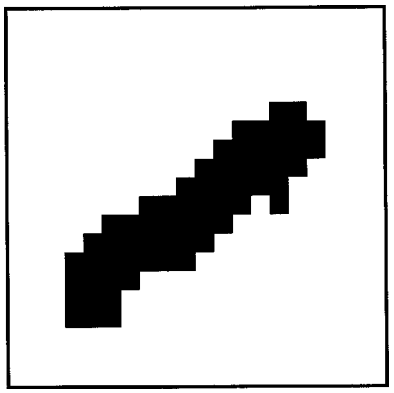

Fig. 11 Input pattern (a 20×20 cell plane).

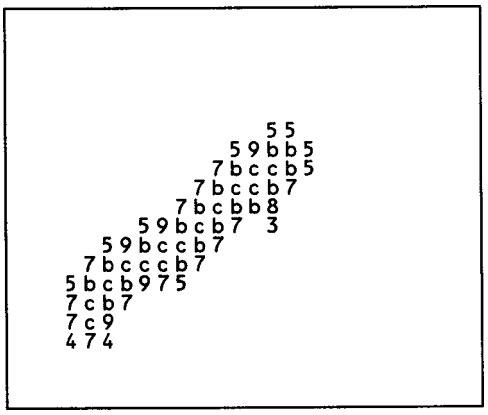

Fig. 13 3-D figure generated by the pattern in Fig. 11.

12) to generate weights for the input pattern. When there is a match using the window patterns in Fig. 12(a), a weight 1 is assigned; otherwise, 0 is assigned when there is no match. Similarly, weight 2 is assigned when there is a match using the window patterns in Fig. 12(b) and weight 0 is assigned when there is no match. Each window pattern matching creates a cell plane. Such weight assignment is generated by using these three window patterns and is the key difference between neocognitron and SC. As a result, there are 20 cell planes generated in the layer S_1. Then the layer C_1 combines the orientation information provided by 20 cell planes in the layer S_1 and merges them into 8 cell planes representing eight different geometric orientations:

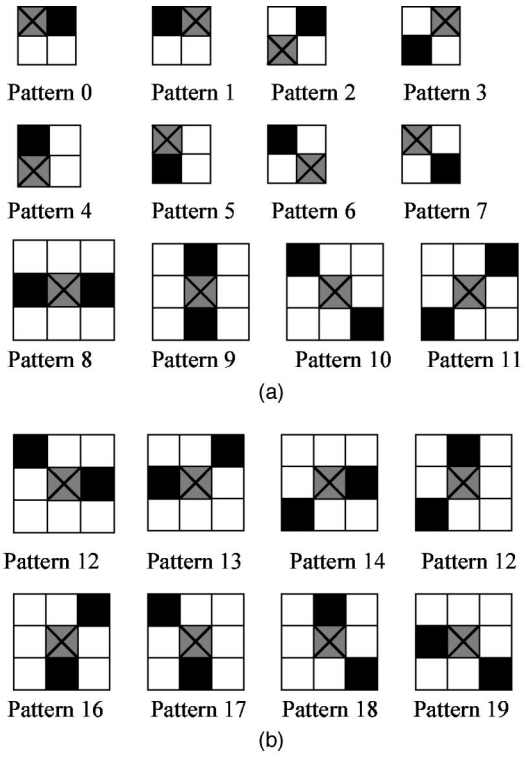

Fig. 12 (a) Masking window spatial patterns for pattern matching using weight 0 or 1 and (b) masking window spatial patterns for pattern matching using weight 0 or 2.

22.5, 45, 90, 135, 180, 225, 270, and 360 deg. Then the C_1 layer can be viewed as a shape orientation fusion layer.

3.1.3 *3-D figure layer of SC*

The layer following the first module (S_1, C_1) is the 3-D figure layer, which has only one 20×20 cell plane resulting from summing up all eight cell planes in the C_1 layer. Since each pixel in any cell plane has a value of 0, 1, or 2, the summed cell plane will take integral values ranging from 0 to 16, which can be viewed as a numeric representation for the pixel. The higher is the numeric value, the more window patterns the pixel matches, and thus the higher value is the shape curvature around this pixel. Using these numeric values as elevations of pixels can create a 3-D figure for the input pattern with the third dimension referred to as the shape curvature dimension. Thus, the elevations of pixels can show their shape curvatures in the 3-D figure model. Accordingly, a 20×20 input pattern can be displayed by a 3-D $20\times20\times h$ figure where $h \in \{0,1,2,...,13\}$, as illustrated in Fig. 13 with an input pattern in Fig. 11. Table 1 tabulates numeric representations obtained from 3-D figures for eight different shape orientations.

3.1.4 *Second module of SC: a combined simple S_2 layer and complex C_2 layer*

Following the 3-D figure layer is a second module (S_2, C_2). The layer S_2 is a shape feature selection layer that produces the 13 primary shape features tabulated in Table 2. These features are suggested in Ref. 25 and extracted from the input pattern based on the shape curvature information provided by the elevations of the 3-D figure in 3-D figure layer. Each of 13 generated shape features represents a specific shape characteristic. They will be used as inputs of C_2 layer. However, it should be noted that since the 13 shape features in Table 2 have different values in various applications, it is not necessary to use up all the 13 shape features. For example, some shape features may be not as important as others in certain applications. As demonstrated in the experiments in Sec. 4, some shape features such as features 1 to 3 are not significant in detection of venous beading, but they were found to be useful for detection of microcalcifications.[25] In general, there is no optimal set of

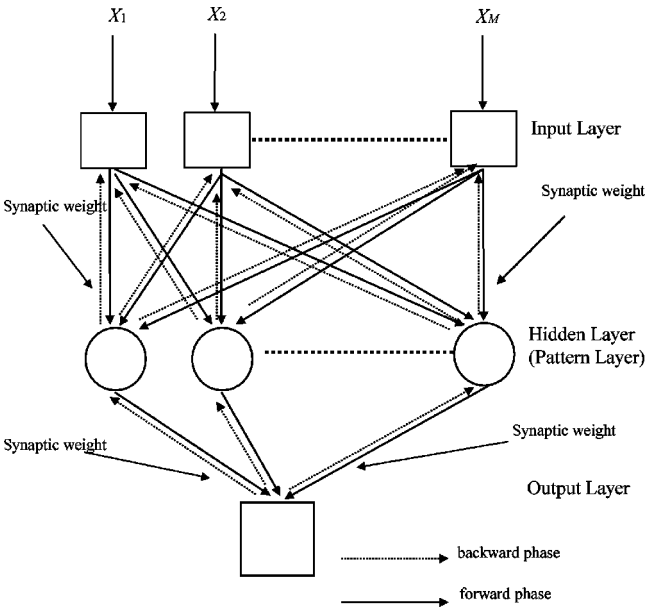

Fig. 14 Structure of BNN.

shape features for the layer C_2. The desired shape features are empirically predetermined based on the characteristics of the input patterns. The layer C_2 can be regarded as a classification or recognition layer. It is a neural-network-based classifier that produces classification results in the output layer. It uses 13 shape feature as inputs with outputs determined by the number of patterns needed to be classified or recognized. It also implements a BNN, which is implemented to perform the classification task. The structure of the BNN is given in Fig. 14. As noted previously, if some shape features are not used, their corresponding weights are simply set to zero to deactivate these features. Since the layer C_2 is an application-dependent layer, it can be designed separately to adapt different needs. In particular, the BNN can be replaced by other neural networks.

3.1.5 *Output layer of SC*

The output layer is the last layer in the SC, which outputs the desired classification results. In this paper, we are interested only in discriminating a beaded vein from a normal vein, so two nodes are used in this layer. Nevertheless, this can be easily extended to more than two classes by including more nodes such as ''normal,'' ''likely,'' ''possible,'' ''probable,'' and ''positive'' to represent different degrees of venous beading.

4 Experiments

To evaluate our proposed system, 61 512×512 gray-scale retinal images were acquired at the Hsin-Chu Public Hospital in Taiwan and used for experiments. These images include 32 venous beaded images and 29 normal images. The regions of interest (ROIs) were selected by experienced doctors and cropped to 180×180 image patterns among which 20 patterns were randomly chosen as training patterns. These training patterns were further split evenly with 10 normal and 10 beaded patterns. Two sets of features were used for the layer C_2 and tabulated in Table 3. Each set consisted of seven shape features. The shape features in these two feature sets generated by the training patterns were used as training data for the BNN implemented in the layer C_2. Table 4 shows the resulting confusion matrix of 41 test patterns produced by the SC for each feature set. The corresponding classification results are also given in Table 5, which shows that feature set 2 produced a better overall classification rate and a lower error rate than did feature set 1. However, it is interesting to note that if we examine Table 4 carefully, feature set 1 seems to be biased toward labeling normal veins as beaded, whereas feature set 2 seems biased toward labeling beaded veins as normal. If in some particular application, there was a high cost to a missed detection (a beaded vein being labeling normal) such as a patient not receiving necessary treatment, feature set 1 might be preferable, since feature set 2 seems to miss some abnormal veins. Note that the classification performance of the SC is heavily determined by the neural network used in the layer C_2 and the feature set generated by the layer S_2 used for training. In the experiments conducted here, we simply used the popular BNN as a classifier rather than designing more sophisticated neural networks. However, the open architecture of the proposed system enables us to replace any component to improve the performance.

Table 3 Two sets of features generated by the layer S_2.

Feature Sets	Features
1	4, 5, 6, 8, 9, 10, and 12
2	4, 5, 7, 8, 9, 11, and 13

Table 4 Results produced by SC.

	Beaded Veins Patterns (22)		Normal Veins Patterns (19)	
Classification Result	Beaded	Normal	Beaded	Normal
Feature Set 1	19	3	4	15
Feature Set 2	17	5	1	18

5 Conclusions

A computer-aided diagnostic system for venous beading detection in retinal images is presented. The system consists of two modules, the BVEM and the VBDM. The BVEM is carried out by four processes in sequence, BSGMF for blood vessel extraction, JRE for segmentation

Table 5 Classification rates produced by SC.

	Classification Rate	
Feature Set	Correction Rate (%)	Error Rate (%)
1	83	17
2	85	15

of extracted blood vessels, morphological operation for edge smoothing and noise suppression, and thinning for bifurcation elimination. The VBDM processes the blood vessels extracted by the BVEM for venous beading detection. To make a reliable diagnosis, the SC is introduced to recognize various shapes of extracted blood vessels (veins). Since the SC has shown potential in an application of microcalcifications classification to capture shape curvatures of clustered microcalcifications, it is modified to recognize shapes of extracted blood vessels. Although the proposed system is still in an early stage and requires more clinical trials to further improve the system, it offers new concepts of designing a computerized venous beading detection system. The preliminary study reported also provides encouraging results for further pursuing.

Acknowledgments

This work was supported in part by a grant from Precision Instrument Development Center, National Science Council, Republic of China. The authors would like to thank two anonymous reviewers for their comments, which helped to improve the paper quality and presentation.

References

1. P. H. Gergson, Z. Shen, R. C. Scott, and V. Kozousek, ''Automated grading of venous beading,'' *Comput. Biomed. Res.* **28**, 291–304 (1995).
2. R. N. Frank, ''Vascular disease of retina,'' in *Retinal Disease-Biomedical Foundations and Clinical Management*, M. O. M. Tso, Ed., pp. 141–142, Lippincott, Philadephia (1988).
3. Diabetic Retinopathy Study Research Group, ''A modification of airlie house classification of diabetic retinopathy,'' *Invest. Ophthalmol. Visual Sci.* **21**, p. 210 (1981).
4. Early Treatment Diabetic Retinopathy Study Group, ''Fundus photographic rsik factor for progression of diabetic retinopathy,'' ETDRS Report no. 12 Phthalmol. **98**, 823–833 (1991).
5. R. M. Haralick, J. S. J. Lee, and L. G. Shapiro, ''Morphological edge detection,'' *International Journal* **3**, 142–155 (1987).
6. K. Akita and H. Kuga, ''Pattern recognition of blood vessel networks in ocular fundus photographs,'' in *Proc. IEEE Int. Workshop Phys. and Eng. in Med. Imaging*, pp. 436–441 (1982).
7. R. Nevatia and K. R. Babu, ''Linear feature extraction and description,'' *Comput. Graph. Image Process.* **13**, 257–269 (1980).
8. M. Tanka and K. Tanka, ''An automatic technique for fundus photograph mosaic and vascular net reconstruction,'' in *Proc. MEDINFO 80*, pp. 116–120, Tokyo (1980).
9. S. Chaudhuri, S. Chatterjee, N. Katz, M. Nelson, and M. Goldbaum, ''Detection of blood vessels in retinal images using two-dimensional matched filters,'' *IEEE Trans. Med. Imaging* **8**, 263–269 (1989).
10. J. Lay and B. Badouin, ''Computer analysis of angioflourograms,'' in *Proc. 7th Int. Conf. Pattern Recognition*, pp. 927–929 (1984).
11. A. V. Cideciyan, ''Registration of ocular fundus images,'' *IEEE Eng. Med. Biol. Mag.* **14**, 52–58 (1995).
12. P. Nagin, B. Schwarz, and G. Raymond, ''Measurement of fluorecein in angiograms of the optic disc and retina using computerized image analysis,'' *Ophthalmology (Philadelphia)* **92**, 547–552 (1985).
13. P. Jasiobedzki, D. Mcleod, and C. J. Taylor, ''Detection of nonperfused zones in retinal iamges,'' in *Proc. Computer-Based Medical System, 4th Annu. IEEE Symp.*, pp. 162–169 (1991).
14. C.-I. Chang, K. Chen, J. Wang, and M. L. G. Althouse, ''A relative entropy-based approach to image thresholding,'' *Pattern Recogn.* **27**, 1275–1289 (1994).
15. C.-W. Yang, P.-C. Chung, C.-I. Chang, J. Wang, and M. L. G. Althouse, ''Entropic and relative entropic thresholding,'' in *Proc. Joint Conf. 1996 Int. Comput. Symp.*, Kaoshiung, Taiwan, ROC, pp. 82–89 (1996).
16. M. Holt, A. Stewart, M. Clint, and R. H. Perrott, ''An improved parallel thinning algorithm,'' *Commun. ACM* **30**(2), 156–160 (1987).
17. S. Tamura, Y. Okamoto, and K. Yanashima, ''Zero-crossing interval correction in tracing eye-fundus blood vessels,'' *Pattern Recogn.* **21**(3), 227–233 (1988).
18. C.-W. Yang, P.-C. Chung, and C.-I. Chang, ''A new neural model for shape recognition: shape cognitron,'' in *Proc. 1996 Int. Symp. on Multi-Technology Information Processing*, pp. 195–200, Kaoshiung, Taiwan (1996).
19. Y. Xu and C.-I. Chang, ''Method and apparatus for automatic pattern recognition,'' U.S. Patent No. 5,784,485 (July 1998).
20. Y. Xu and C.-I. Chang, ''Implementation of a 3-D model for neocognitron,'' in *Proc. Int. Conf. Neural Networks*, pp. 794–799, Washington, DC (1996).
21. B.-C. Hsu, P.-C. Chung, and C.-I. Chang, ''Automated system for detection and classification of microcalcifications in digital mammograms,'' in *Proc. CVGIP'96*, pp. 127–134 (1996).
22. D. J. Ma, S.-C. Chao, C.-W. Yang, and C. H. Wen, ''A bell-shaped matched filter approach to blood vessel detection in retinal images,'' in *Proc. IASTED Int. Conf. Signal and Image Processing*, pp. 1127–1140, New Orleans, LA (1997).
23. T. Cover and J. Thomas, *Elements of Information Theory*, John Wiley & Sons, New York (1991).
24. K. Fukushima and N. Wake, ''Handwritten alphanumeric character recognition by the neocognitron,'' *IEEE Trans. Neural Netw.* **2**(3), 355–365 (1991).
25. P. C. Hsu, *An Automatic System for Detection and Classification of Microcalcifications in Digital Mammograms*, MS Thesis, Department of Electrical Engineering, National Cheng Kung University, Tainan, Taiwan (June 1996).

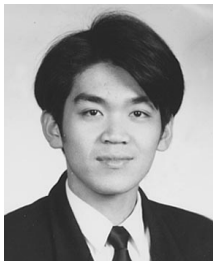

Shuenn-Ching Chao received his BS degree in computer science and information engineering from Yuan-Zi University, Chung-Li, Taiwan, in 1995 and his MS degree in applied mathematics from National Chung-Hsing University, Taichung, Taiwan, in 1997. Since July 1999, he has been with ARES International Corp., Taipei, Taiwan, working on network management systems. His research interests include computer networks, neural networks, and medical image processing.

Chia-Hsien Wen received his BS degree in computer sciences from Tang Kang University, Taiwan, in 1972 and his MS degree in applied mathematics and his PhD degree in computer science from National TsingHua University, Taiwan, in 1978 and 1994, respectively. He currently directs the Computer and Communication Center at Taichung Veterans General Hospital, Taiwan. His research interests include image processing, biomedical image processing, and artificial intelligence.

Biographies and photographs of other authors appear in the paper ''Generalized constrained energy minimization approach to subpixel target detection for multispectral imagery'' in this issue.